ACS Biomaterials SCIENCE & ENGINEERING

pubs.acs.org/journal/abseba

Article

Three-Dimensional-Printed Flexible Scaffolds Have Tunable Biomimetic Mechanical Properties for Intervertebral Disc Tissue Engineering

Samantha L. Marshall, Timothy D. Jacobsen, Erik Emsbo, Archana Murali, Kevin Anton, Jessica Z. Liu, Helen H. Lu, and Nadeen O. Chahine*

Cite This: *ACS Biomater. Sci. Eng.* 2021, 7, 5836–5849

Read Online

ACCESS | Metrics & More | Article Recommendations | Supporting Information

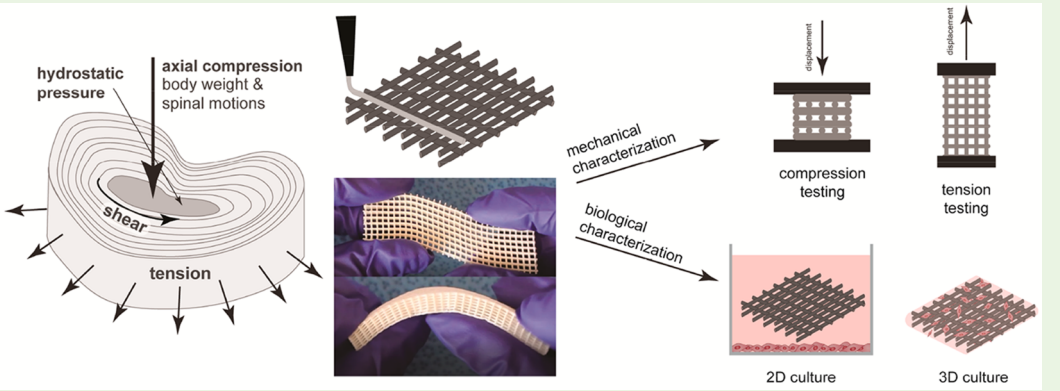

ABSTRACT: The intervertebral disc (IVD) exhibits complex structure and biomechanical function, which supports the weight of the body and permits motion. Surgical treatments for IVD degeneration (e.g., lumbar fusion, disc replacement) often disrupt the mechanical environment of the spine which lead to adjacent segment disease. Alternatively, disc tissue engineering strategies, where cell-seeded hydrogels or fibrous biomaterials are cultured *in vitro* to promote matrix deposition, do not recapitulate the complex IVD mechanical properties. In this study, we use 3D printing of flexible polylactic acid (FPLA) to fabricate a viscoelastic scaffold with tunable biomimetic mechanics for whole spine motion segment applications. We optimized the mechanical properties of the scaffolds for equilibrium and dynamic moduli in compression and tension by varying fiber spacing or porosity, generating scaffolds with *de novo* mechanical properties within the physiological range of spine motion segments. The biodegradation analysis of the 3D printed scaffolds showed that FPLA exhibits lower degradation rate and thus has longer mechanical stability than standard PLA. FPLA scaffolds were biocompatible, supporting viability of nucleus pulposus (NP) cells in 2D and in FPLA+hydrogel composites. Composite scaffolds cultured with NP cells maintained baseline physiological mechanical properties and promoted matrix deposition up to 8 weeks in culture. Mesenchymal stromal cells (MSCs) cultured on FPLA adhered to the scaffold and exhibited fibrocartilaginous differentiation. These results demonstrate for the first time that 3D printed FPLA scaffolds have *de novo* viscoelastic mechanical properties that match the native IVD motion segment in both tension and compression and have the potential to be used as a mechanically stable and biocompatible biomaterial for engineered disc replacement.

KEYWORDS: *Intervertebral disc, 3D printing, Biomaterials, Scaffold, biomechanics*

1. INTRODUCTION

Back pain, one of the most common reasons for doctor visits and the leading cause of disability, has been associated with degeneration of the intervertebral discs.[1−3] The intervertebral disc (IVD), the connective tissue between vertebral bodies, is a complex load bearing composite tissue populated by a relatively low density of mechanosensitive cells.[4] The inner nucleus pulposus (NP) region is surrounded by an outer annulus fibrosus (AF) region (Figure 1a). The NP is composed of a highly hydrated gelatinous matrix made up of negatively charged proteoglycans, collagen, and noncollagen proteins, which bears high axial compressive and osmotic stresses.[5,6] Degradation of the NP is characterized by elevated catabolic activity that reduces proteoglycan levels and drives changes in the tissue

Received: October 15, 2021
Accepted: November 8, 2021
Published: November 29, 2021

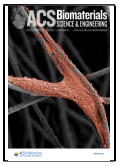

https://doi.org/10.1021/acsbiomaterials.1c01326
ACS Biomater. Sci. Eng. 2021, 7, 5836−5849

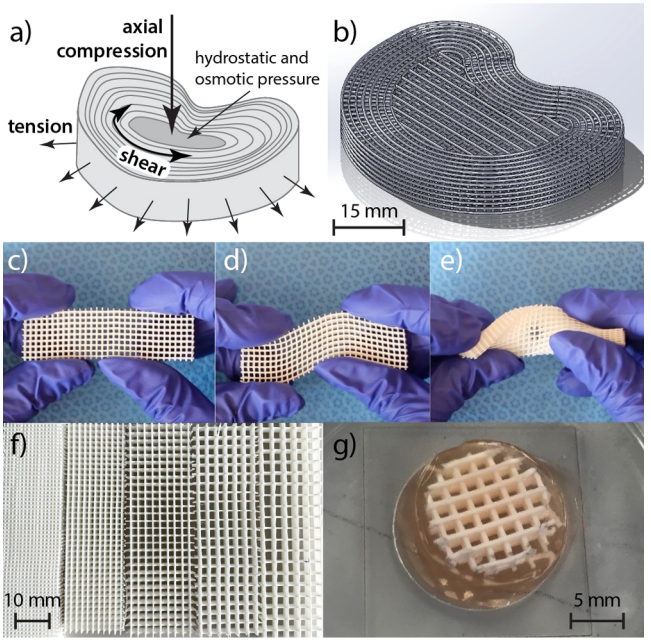

Figure 1. (a) Schematic showing loading of the intervertebral disc. (b) CAD render of an FPLA IVD shape. (c–e) Still images extracted from a video showing (c) FPLA sheet, (d) bent FPLA sheet, and (e) twisted FPLA sheet. (f) FPLA scaffolds with different fiber spacing (1, 1.5, 2, 2.5, and 3 mm). (g) Printed 1.5 mm FPLA scaffold filled with 1.2% alginate and bovine NP cells.

structure, such as loss of disc height and reduced hydration.[7−9] The AF is comprised of aligned collagen fibers that resist high expansion tensile stress in the radial direction.[10]

The multiaxis mechanical properties of the native IVD are complex and require a delicate balance between the different regions of the IVD.[6,11−15] Briefly, body weight and spinal motion cause longitudinal (axial) compression of the motion segment, which promotes generation of hydrostatic pressure within the NP. This is counterbalanced by radial tension and circumferential shear within the AF.[16−20] Additionally, the tissue is viscoelastic and therefore its response to loading is time dependent.[10,16,21−23] While independent mechanical properties of the NP and AF are known, for the purpose of designing engineered replacement materials, motion segment mechanics may be the more important functional unit, as they represent the macroscopic tissue response.[11] When aiming to replace the entire disc space, the goal is to match the physiological mechanical environment of the IVD. Representative benchmark properties from literature are shown in Table 1 and represent a standard in the field for which biomaterials are assessed against.[11]

Currently, the treatment paradigm for painful degenerated disc is to perform a spinal fusion or total disc replacement.[27−29] In both approaches, the native disc tissue is removed and replaced with either a metal cage containing bone grafts to promote fusion, or with a motion preserving artificial disc implant. Despite the vast differences in how these surgical treatments work, both are associated with complications in the surrounding tissues due to disruption of the mechanical environment in the spine that can result in reoperation.[30,31] Adjacent segment disease, characterized by degeneration of IVD segments adjacent to the fused spinal level, is commonly observed.[32−36]

Table 1. Benchmark Mechanical Properties for Intervertebral Disc Replacement

	equilibrium modulus	dynamic modulus
compression (motion segment)	3−10 MPa[11]	∼30 MPa[24]
tensile (annulus fibrosus−multiple lamella)	10−45 MPa[21,25]	1−5 MPa[26]

As an alternative to current surgical treatment approaches, tissue engineering of the IVD has been an area of significant research. The aim of most studies involving tissue engineering biomaterials is to recapitulate the properties of either the AF or the NP separately. Commonly used biomaterials for NP replacement include soft hydrogels such as alginate or hyaluronic acid,[38−44] whereas AF replacement is typically approximated using aligned fiber materials like electrospun polycaprolactone (PCL) or collagen.[37,45−52] Additional parameters to be considered include degradation rates, biocompatibility, host tissue interaction, mechanical stability, optimal pore size, surface area, protein coating, mechanical properties, and diffusivity.[37]

Several studies have combined two different biomaterials to create an engineered whole disc replacement.[37,53−61] One composite whole disc replacement, using PLA mesh for the AF and alginate gel for the NP, exhibited increased ECM over time *in vitro*, some integration between the two regions after 12 weeks in culture, an increase in mechanical properties over time, and shows promise in maintaining disc height in an animal model.[56,62] Another composite whole disc replacement using electrospun PCL for the AF and agarose for the NP[37] observed compressive stress relaxation behavior and an increase in compressive modulus over weeks in culture. Additional animal studies of this implant highlighted the need for integration into the surrounding anatomy, so engineered end plates of an additional material were added to the design.[53,63] These types of complex tissue engineered whole disc approaches recapitulate anatomical and some mechanical properties of the disc and show promise for restoring disc height.[53] Despite the progress on tissue engineered whole disc replacements, these approaches are limited translationally because of the required extensive preimplantation duration needed for cell culture to promote ECM synthesis and equilibrium mechanical properties that approach biomimetic disc levels. Additional maturation for 10−20 weeks *in vivo* was required in one study to reach native equilibrium properties.[53] Functional dynamic properties of the engineered discs are not typically characterized, and it remains unknown how closely engineered discs recapitulate the native motion segment dynamic mechanical properties. Moreover, the success of composite whole disc strategies is dependent on successful integration between component regions. As failure theory dictates, most failures occur at the interface of dissimilar materials. In this context, the interfaces between the NP and AF regions and the between the IVD and adjacent bones are critical to minimize implant failure.[54] Successful implantation of a mechanically premature IVD scaffold has been achieved with the use of external or internal fixators/plates to augment *in vivo* disc repair in some preclinical studies partly to prevent disc height collapse.[37,63,64] Indeed, the need and use of fixator devices for success of the whole disc tissue engineering implants diminishes the value of having a biological motion preserving engineered disc design.

There is a technical gap and a scientific need for scaffolds that serve as a mechanical mimic of the spinal motion segment.

https://doi.org/10.1021/acsbiomaterials.1c01326
ACS Biomater. Sci. Eng. 2021, 7, 5836−5849

Three-dimensional printing allows for spatial control of material deposition as well as creation of complex shapes, enabling printed structures that have varying material properties across the structure. Within the IVD paradigm, this can allow for differing properties in the AF region versus the NP region, as well as structures for optimal integration all created in one uniform process. However, conventional 3D printed materials have nonphysiological material properties. Materials such as ABS and PLA are too stiff compared to IVD tissues,[65−67] and 3D printed polyurethane or hydrogels are too soft.[68,69] In this study, we employ a novel polymer (FPLA) composed of polylactic acid (PLA) and an elastomer for 3D printing scaffolds that mimic the mechanical properties of the spine motion segment. The goal is to create biocompatible flexible polymer scaffolds that will mimic both the equilibrium and dynamic material properties *de novo* without the need for extended culture time preimplantation. We hypothesize that 3D printing FPLA scaffolds will yield tunable mechanical properties within the physiological range of compressive mechanical properties of full IVD motion segments and tensile mechanical properties of the AF. These mechanical benchmarks were selected because the spinal motion segment is subjected to compressive stress, while the AF is exposed mainly to high levels of tensile stress. Therefore, they represent the greatest demands from a material property perspective. In addition to optimizing the equilibrium and dynamic mechanical properties of FPLA 3D printed scaffolds in compression and in tension, we also evaluated the degradation behavior of FPLA in comparison to PLA, assessed biocompatibility, and demonstrated the ability of FPLA scaffolds to promote fibrocartilaginous differentiation. In some studies, composites of FPLA and alginate were evaluated for proteoglycan-rich matrix deposition and to determine contribution of the two components on scaffold mechanics. We also produced 3D printed anatomical IVDs containing an AF and NP region and evaluated their biomechanical properties compared to native lumbar bovine discs.

2. MATERIALS AND METHODS

2.1. Scaffolds. Scaffolds were printed from FlexiFil PLA (FPLA), a thermoplastic copolyester elastomer/polymer blend (FormFutura) with reported tensile modulus of 95 MPa, using a Makerbot Replicator plus 3D printer (Makerbot) and a Makerbot Experimental Extruder with 0.4 mm print nozzle. Tape was used to adhere the scaffold to the bed of the printer during printing to avoid warping of the structure. In pilot tests, we investigated a range of printing temperatures and speeds, and ultimately employed an extrusion speed of 90 mm/s at an extruder temperature of 245 °C. Scaffold strands were deposited layer by layer with alternating 0°/90° lay-down pattern producing a continuously interconnected scaffold with tetragon shaped pores. Scaffolds were printed with varying fiber spacing of 1, 1.5, 2, 2.5, 3 mm (Figure 1b−f). Scaffold sample geometry varied based on testing methods. Square compression testing samples were used with cross section of 15 mm × 15 mm and 6 mm height to allow a large enough cross section for testing all the fiber spacings used, but limited to fit under the stainless steel compression platens. The height of 6 mm was chosen because it mimics the height of large animal lumbar discs or human cervical discs.[70,71] For tensile testing, rectangular samples 40 mm length × 15 mm width × 6 mm depth were used. While dogbone-shaped samples are commonly used in tensile testing (particularly for failure analysis), their utility for 3D printed FPLA samples was limited because the dogbone geometry would disrupt the rectilinear fiber alignment and fiber density pattern used in the study, without providing significant additional testing benefit in characterizing material properties of FPLA. Indeed straight sided samples are commonly used in biomaterial mechanical characterization and this geometry is permitted in ASTM standards.[72,73]

The effective scaffold porosity was also quantified for the rectilinear FPLA samples.[74] Porosity (ϵ) was computed as the ratio of the apparent volume to the true volume, such that $\epsilon = 1 - m/V\rho \times 100$, where ρ is the density of FPLA (ρ = 1.14 g/cm^3, as reported by the manufacturer). Sample volume (V) was calculated from sample dimensions measured with digital calipers. Sample mass (m) was determined by weighing the samples. N = 3 samples per fiber spacing were used to determine porosity. The resulting effective porosity was analyzed as a function of fiber spacing using nonlinear regression (log−log fit) using GraphPad Prism, and the slope of the resulting power law was computed.

To evaluate resulting fiber dimensions of the 3D printed scaffolds, samples were scanned using μCT and then analyzed. Scans were performed on a SkyScan 1272 (Bruker) with a pixel size of 18 μm, power of 40 kV, image size of 1344 × 896, and no filter was used. Frames were averaged three times to remove any background. Reconstructions were performed using SkyScan NRecon, 3D models were visualized in CTvol, and CTAn was used to select a representative image from each scaffold. ImageJ was used to compute the fiber diameter across an image from each scaffold and the mean diameter and standard deviation were computed.

2.2. Mechanical Characterization of FPLA Scaffolds. For evaluation of equilibrium mechanical properties in compression, constructs were tested on a TA Electroforce DMA 3200 Mechanical Tester, where the force and displacement data were recorded using the accompanying WinTest software. For unconfined compression testing, samples (15 mm × 15 mm × 6 mm) were compressed between two stainless steel platens. A 0.5N preload was first applied, followed by a stress relaxation test, where compression was applied at a rate of 1 mm/min up to a maximum strain of 25% initial thickness (n = 4 per fiber spacing). Equilibrium compressive modulus was computed as the ratio of stress to strain at equlibrium. For tensile testing, samples were tested using an Instron material test frame (Instron 5566), where the force and displacement were recorded using the accompanying BlueHill software. Constructs (40 mm × 15 mm × 6 mm) were clamped into tensile grips, and a 0.5N preload was applied. A ramp stretch of 20% was then applied at a rate of 1 mm/min. The tensile modulus was computed as the ratio of stress to strain at equilibrium (n = 4 per fiber spacing). Additional select evaluations of equilibrium tensile properties were performed using the TA Electrofoce tester with the same protocol.

Compressive (n = 14) and tensile (n = 4) dynamic mechanical analysis (DMA) testing was performed using a TA Electroforce DMA 3200 Mechanical Tester. A 5N preload was applied to each sample. For compressive testing, samples were then loaded between two stainless steel platens first with a 10% static strain ramp followed by 10% cyclic compression (ranging from 5% to 15% strain) applied with a frequency sweep ranging from 0.1 to 10 Hz. For tensile testing, samples were gripped in a vise grip at an initial length of 20 mm and subjected to a 5N preload. Samples were then loaded with a 15% tensile strain ramp followed by 10% cyclic stretch (ranging from 10% to 20% strain) applied with a frequency sweep from 0.1 to 10 Hz. Dynamic modulus and phase angle were calculated using the DMA software. The dynamic modulus is calculated as the ratio of the force to displacement over a shape factor (rectangle = (length)(width)/height). The phase angle is calculated as the shift offset between the displacement and force curves.[75]

2.3. Biodegradation. To monitor the stability of the FPLA scaffold over time, biodegradation tests were performed in conditions that mimic *in vivo* setting. The primary mechanism of PLA degradation is hydrolysis, and temperature increases the rate of degradation.[76] Samples with a fiber spacing of 1, 1.5, 2, 2.5, and 3 mm were evaluated (n = 3 per spacing group). Samples were incubated in PBS at 37 °C for up to 34 weeks. Every 2 weeks, the samples were removed from the PBS bath, dried, weighed to determine mass loss. As a comparator, PLA scaffolds with spacings of 1, 2, and 3 mm were also subjected to the same degradation protocol and were analyzed for mass loss. FPLA samples were also subjected to compressive DMA testing (as described above), and scanned in a μCT to evaluate any mechanical degradation or morphological changes over time, respectively. Scans were performed as described above.

https://doi.org/10.1021/acsbiomaterials.1c01326
ACS Biomater. Sci. Eng. 2021, 7, 5836−5849

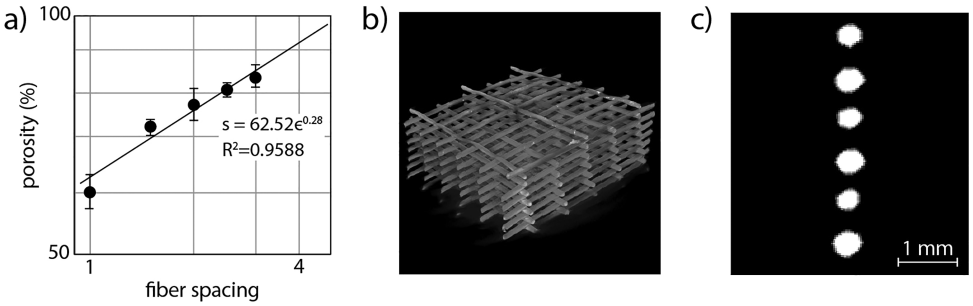

Figure 2. Scaffold porosity and diameter characterization. (a) Log−log scale graph of porosity (ε) versus fiber spacing (s) scaling. (b) Representative μCT of FPLA 3D printed scaffold with 1.5 mm fiber spacing. (c) Cross-sectional view of μCT scan of 3D printed FPLA fibers was used to measure fiber diameter.

2.4. Bovine *Ex Vivo* Testing and Anatomical Disc Design. Bovine lumbar spine motion segments (n = 4) were isolated and individual bone−disc−bone motion segments were generated. Samples were dissected down to remove all adjacent bone and end plates. The segments were tested under unconfined compression in a PBS bath using a testing protocol used to evaluate intradiscal pressure.[77] Samples were preloaded with 50N force for 15 min, then a ramp to 250N was applied with ±20N applied cyclically (0.1 Hz) for 45 min. The instantaneous modulus was computed as the loading ramp modulus after preload and the equilibrium modulus was computed as the average modulus after 45 min of cyclic loading.

On the basis of average bovine IVD dimensions, a CAD model was designed for 3D printing in FPLA (Figure 1b) with a height of 5.5 mm, lateral width of 41 mm, and cross-sectional area of 1185 mm^2. The NP region lateral width was 27 mm which was created with 2.0 mm fiber spacing. The width of the AF region was 8 mm, printed with 1.0 mm fiber spacing. The outer edges of the biomimetic scaffold were rounded in the design to follow a contour similar to a native IVD. The models were printed using the same printing parameters described above. The 3D printed anatomical discs were mechanically tested using the same physiological testing protocol used on bovine discs.

2.5. Biomechanics of FPLA Scaffolds with Alginate. To determine the potential contribution and interaction between FPLA scaffold and a hydrogel, FPLA scaffolds were tested with or without alginate. To create the composites, 1.2% sterile-filtered alginate (in NaCl+HEPES solution) was placed within a circular 10 mm rubber mold. FPLA scaffolds (1.5 mm spacing, 3 mm in height, and 10 mm in diameter) were bathed in $CaCl_2$ solution then carefully transferred and pressed into the alginate-filled mold; a small drop of $CaCl_2$ was placed on top of the scaffolds to ensure even curing. Alginate only groups were cured in the same size molds with a filter paper on top to promote even dispersion of the $CaCl_2$ solution. Constructs were allowed to cure for 30 min before being transferred to a NaCl+HEPES bath to incubate overnight.

To determine equilibrium modulus and instantaneous modulus, FPLA scaffolds (1.5 mm spacing, 3 mm height, 10 mm diameter) with and without alginate and alginate alone (n = 4) were subjected to a multistep stress relaxation testing protocol. Samples were incrementally compressed under unconfined compression from 5% strain to 25% strain in steps of 5% strain. Instantaneous modulus was calculated by determining the peak stress at each strain point and fitting a line through the stress versus strain values. Equilibrium modulus was determined using the same process for the equilibrium stress at each step. Samples additionally underwent DMA testing consisting of 10% cyclic compression at 1 Hz frequency. For failure testing, samples were preloaded to 0.5 N and were then subjected to a compressive displacement applied at 0.005 mm/s to 2.5 mm. Toughness was calculated as the area under the stress−strain curve leading up to the failure point. A failure criteria was used for ensuring consistency across groups and was defined as the point when the stress rapidly dropped by 15 kPa or more with increasing compression.

2.6. NP Cell Isolation and Culture in 2D Culture and on 3D Composite Scaffolds. NP tissue was dissected from five healthy bovine lumbar spines under sterile conditions. Tissue was digested with Collagenase-type I (0.3 mg/mL) and Collagenase-type II (0.3 mg/mL) for 4 h under agitation to isolate NP cells. Primary NP cells were seeded in scaffolds immediately after isolation. In some experiments (2D cytotoxicity experiments and mechanical testing of cell seeded scaffolds) primary NP cells were expanded in monolayer in DMEM +10%FBS+1%AA up to passage 2 before use. In all other experiments, primary NP cells were used.

For evaluating initial biocompatibility of the scaffolds, NP cells were seeded into 24 well plates for 24 h. 3D printed scaffolds (15 mm × 15 mm × 6 mm, 2 mm spacing) were sterilized with an ethanol soak followed by a saline rinse. Scaffolds were then added to each cell seeded well for a duration of 3 weeks. NP cells cultured without scaffolds were used a control group. After 3 weeks, scaffolds were removed and cell viability was assessed with Live/Dead staining. Cells were stained with 4 μM Calcein AM (green) and 2 μM Ethidium Homodimer-1 (red) and imaged on a confocal microscope to determine cytotoxicity with green indicative of live cells and red representing the nuclei of dead cells (n = 3 samples per group with three images acquired per sample). In some studies, bone marrow derived mesenchymal stem cells (MSCs) were seeded on FPLA alone or FPLA+alginate up to 7 days in culture. Viability was evaluated using Live/Dead staining at day 1 (see Supporting Information). DNA content (PicoGreen dsDNA assay) and fibrocartilaginous differentiation were evaluated using gene expression analysis collagen-1 (COL1A), collagen-2 (COL2A), and aggrecan (ACAN) (Figure S2).

For evaluating response of NP cells in 3D FPLA composites, bovine NP cells (2 million cells/mL) were cast in 1.2% alginate in the FPLA scaffolds. FPLA scaffolds (1.5 mm spacing) were sterilized by autoclave prior to casting. 1.2% sterile-filtered alginate (in NaCl+HEPES solution) was mixed with cells and cured following the above method. FPLA+alginate molds were incubated at 37 °C and 5% CO_2 for 30 min. After 30 min, the cured scaffolds were removed from the molds and washed three times in NaCl solution before being transferred to a 12 well plate with chondrogenic media, composed of high glucose DMEM (Gibco) supplemented with 1% antibiotic/antimycotic (Corning), 1% insulin-transferrin-selenous acid (ITS+3) liquid media supplement (Sigma), 4 mM L-Glutamax (Gibco), 0.1 μM dexamethasone (Sigma), 50 μg/mL ascorbic acid (Sigma), 40 μg/mL L-proline (Sigma), and 10 ng/mL TGF-β3 (R&D Systems)).[78] The final construct dimensions were 3 mm height and 10 mm diameter.

2.9. Analysis of NP Cell-Seeded Scaffolds. To check cell viability after 2 weeks in culture, cell-seeded scaffolds were collected from culture and stained with Live/Dead stain (4 μM Calcein AM (green) and 2 μM Ethidium Homodimer-1 (red)) for 1 h and imaged on an inverted fluorescent microscope. For biochemical assays, the alginate was dissolved using sodium citrate; the cells were pelleted and digested with papain. Glycosaminoglycan (GAG) content and DNA content were measured using the DMMB assay (1.5 pH)[79,80] and Pico Green assay (Thermo Fisher), respectively (n = 6 for week 0 and 2 time points; n = 8 for week 4 time point), and results are reported as GAG content normalized to DNA content within each sample. For histology, scaffolds were fixed with 4% paraformaldehyde (PFA) overnight, transferred to 70% ethanol, embedded in paraffin, and sectioned at 7

https://doi.org/10.1021/acsbiomaterials.1c01326
ACS Biomater. Sci. Eng. 2021, 7, 5836−5849

μm. Sections were stained with either hematoxylin and eosin (H&E) or Alcian Blue (pH = 1.0). To evaluate mechanical stability in culture, FPLA-alginate scaffolds seeded with 1 million cells/mL (as described above) underwent equilibrium compression testing and compressive DMA testing at 2, 4, and 8 weeks in culture (n = 3 per time point) following the same protocols as cell free scaffold testing described above.

3. STATISTICAL METHODS

For testing the effect of spacing on equilibrium modulus, an ANOVA was performed with Tukey's multiple comparison post hoc test. For testing effect of spacing and frequency on dynamic modulus and phase angle, a two-way ANOVA was used with Fisher's LSD post hoc test. For testing effect of spacing and time on dynamic modulus and weight loss in degradation studies, a two-way ANOVA was used with Fisher's LSD post hoc test. In NP-seeded FPLA/alginate composites, the change in equilibrium modulus, dynamic modulus, phase angle, and GAG content (per DNA) was compared to day 0 using Student t tests. For comparing differences between bovine discs and anatomically shaped 3D printed FPLA discs, Student t tests were performed. For comparing mechanics of FPLA, alginate, and FPLA+alginate, an ANOVA with Tukey's post hoc test was performed. Student t tests and ANOVAs were performed in GraphPad Prism. Two-way ANOVAs were performed in STATISTICA. In all analyses, $p < 0.05$ was considered significant.

4. RESULTS

4.1. Scaffold Properties. The effective porosity of FPLA scaffolds increased nonlinearly with increasing fiber spacing, with values ranging from approximately 60% to 85% porosity (Figure 2a, 1 mm: 60.1 ± 2.9%; 1.5 mm: 72.3 ± 1.7%; 2 mm: 77.4 ± 3.6%; 2.5 mm: 80.6 ± 1.8%; 3.0 mm: 84.0 ± 2.7%). The nonlinear regression of porosity versus fiber spacing using a log−log fit yielded a power law scaling relationship with power = 0.28 (R^2 = 0.958, Figure 2a). μCT analysis of FPLA scaffolds were performed to quantify the resulting fiber diameter (Figure 2b). Cross sectional area analysis of the μCT images using ImageJ (Figure 2c) demonstrated that the effective fiber diameters were 458.2 ± 35.6 μm, when using an extruder with 400 μm nominal print nozzle tip.

4.2. Compressive Properties. The compressive equilibrium modulus of FPLA scaffolds significantly decreased with increasing fiber spacing. Compressive equilibrium moduli ranged from 0.29 ± 0.009 MPa (3 mm spacing) to 4.5 ± 0.4 MPa (1.0 mm spacing, Figure 3a). The equilibrium compressive modulus exhibited a significant inverse relationship with scaffold porosity (R^2 = 0.9572, p = 0.0038, Figure S1a). Equilibrium compression testing of standard PLA scaffolds at 2 mm spacing yielded a compressive modulus of 80.1 ± 4.2 MPa, which was significantly stiffer than FPLA scaffolds of the same spacing (0.65 ± 0.16 MPa, $p < 10^{-5}$, Figure 3a). For dynamic compressive modulus, all spacings resulted in significantly different moduli from one another ranging from a mean of 8.8 ± 1.1 MPa (1 mm spacing) to 0.8 ± 0.2 MPa (3 mm spacing) when averaged across all frequencies tested ($p < 10^{-5}$, Figure 3b). The dynamic compressive modulus for 2, 2.5, 3 mm spacings had a similar magnitude across the tested frequencies ($p > 0.2$); whereas scaffolds with 1 mm and 1.5 mm spacings exhibited changes in dynamic compressive modulus with increasing frequency (Figure 3b) ($p < 0.0001$). The increases in dynamic modulus over the three frequency decades were 23% and 4% for 1 mm and 3 mm scaffolds, respectively. The phase angle was also measured during the dynamic compressive testing, which ranged between 5 and 10° (Figure 3c). Overall, the compressive phase angle had a U-shape pattern with increasing frequency, and phase angle magnitudes increased with increasing fiber spacing.

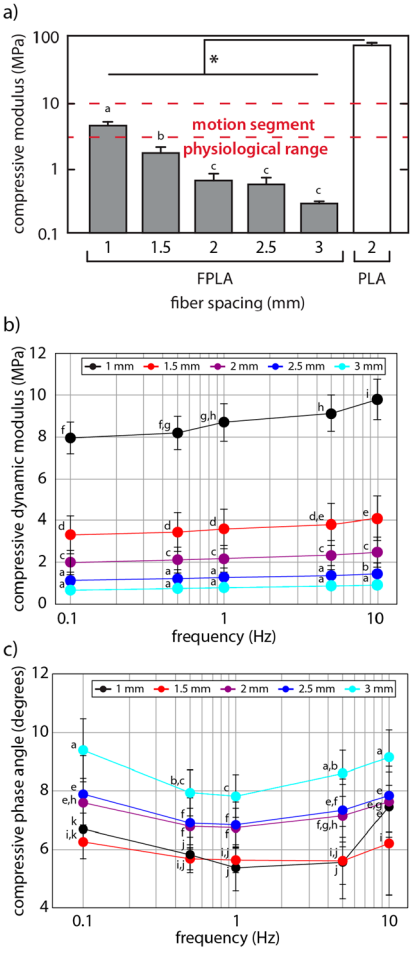

Figure 3. Compressive mechanical properties of FPLA scaffolds. (a) Equilibrium compressive modulus of FPLA and PLA scaffolds with varying fiber spacing. The same letter indicates data points are comparable ($p > 0.05$) and * = significant difference between all FPLA spacings and PLA. (b) Dynamic compressive modulus and (c) phase angle of FPLA scaffolds of varying spacing over a physiological range of frequencies. The same letter indicates data points that are comparable ($p > 0.05$) across either spacing or frequency.

Scaffolds with 3 mm spacing had a significantly higher phase angle than all other spacings ($p < 10^{-5}$), while the 1 and 1.5 mm spacings had the lowest phase angle.

4.3. Tensile Properties. Equilibrium tensile properties showed significant decrease ($p < 10^{-5}$) with increasing fiber spacing between 1, 1.5, 2, and 2.5 mm scaffolds (Figure 4a). Three millimeter scaffolds showed a decreasing trend from 2.5 mm scaffolds (p = 0.17). The 1 and 1.5 mm spacings were within the physiological range for multilamellar AF (10−45 MPa) with moduli of 15.8 ± 1.2 and 13.8 ± 0.8 MPa, respectively,[21,25] while the 2 mm (8.0 ± 0.3 MPa), 2.5 mm (4.7 ± 0.8 MPa), and 3 mm (3.9 ± 0.5 MPa) spacings had tensile moduli within an order of magnitude of the physiological range. The equilibrium tensile modulus exhibited a significant inverse relationship with scaffold porosity (R^2 = 0.8757, p = 0.019, Figure S1b). The dynamic tensile modulus, which ranged between 3 and 11 MPa, was highly dependent on fiber spacing, and the modulus from each fiber spacing was statistically significant from all other spacings ($p < 10^{-5}$). At frequencies ≤1 Hz, the modulus of 2 mm and 2.5 mm fiber spacing scaffolds were comparable. All fiber spacings showed increasing dynamic modulus with increasing frequency

https://doi.org/10.1021/acsbiomaterials.1c01326
ACS Biomater. Sci. Eng. 2021, 7, 5836−5849

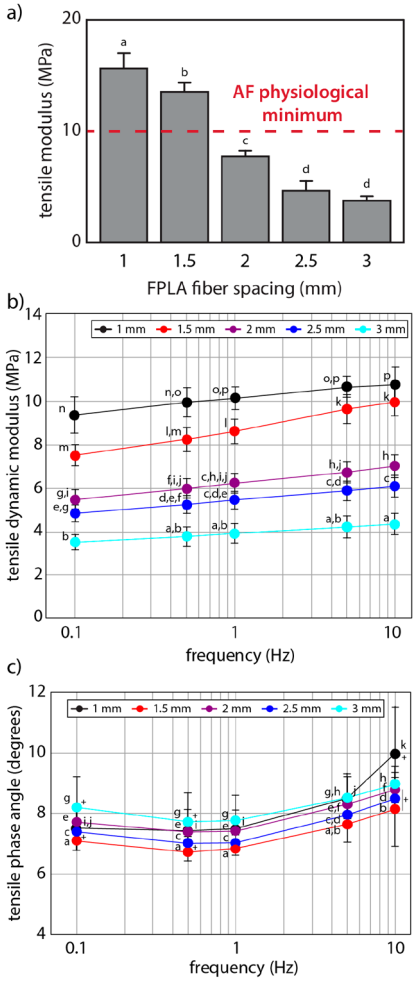

Figure 4. Tensile mechanical properties of FPLA scaffolds. (a) Equilibrium tensile modulus of FPLA scaffolds with varying fiber spacing. The same letter indicates data points that have comparable values ($p > 0.05$) (b) Dynamic tensile modulus and (c) phase angle of FPLA scaffolds of varying spacing over a physiological range of frequencies. The same letter indicates data points that are comparable ($p > 0.05$) across either spacing or frequency. For the phase angle, all spacings were comparable ($p > 0.05$) across frequencies except for 1.5 mm and 3 mm at 0.1 and 0.5 Hz and 1 mm at 10 Hz (statistically different from 1.5, 2, and 2.5 at 10 Hz) as denoted with "+".

(Figure 4b). The 1.5 mm spacing exhibited an increase of 32% in modulus, the greatest increase over three decades of frequency, whereas the 1 mm scaffolds showed the smallest increase of 15%. All phase angles measured were between 6 and 10° (Figure 4c). Spacing was found to be a statistically significant variable contributing to phase angle ($p = 0.007$). In post hoc comparisons, the 1.5 mm and 3 mm spacings were significantly different at lower frequencies (0.1 and 0.5 Hz) and the 1 mm spacing was statistically different than the 1.5, 2, and 2.5 mm spacings at 10 Hz. The five spacings tested all exhibited a similar trend: the phase angle was similar for 0.1, 0.5, and 1 Hz frequency, followed by an increase in phase angle between 1 and 10 Hz (Figure 4). All spacings had a significantly different phase angle for frequencies ≤1 Hz compared to measurements made at >1 Hz ($p < 0.05$).

4.4. Degradation Properties. To assess potential degradation of the FPLA scaffolds, scaffold mass loss was measured over 34 weeks in conditions mimicking *in vivo* (hydrated, ionic environment at 37 °C), and found little change (<2%) in the weight of the FPLA scaffolds (Figure 5a). Scaffolds from all fiber spacings showed an average decrease in weight of 1.35 ± 1.03% at 34 weeks. In post hoc test, no spacing showed significant differences over time. Greater mass loss and measurement variation (i.e., standard deviation) were observed at later time points due to the loss of an entire fiber in a single scaffold sample. As a comparator, weight loss of PLA scaffolds was also evaluated and we found little change in weight of the PLA scaffolds up to 23 weeks. However, at 26 weeks PLA scaffolds had a brittle catastrophic failure (Figure 5b), whereas the FPLA scaffolds maintained their integrity until the end of the experimental duration (34 weeks).

Dynamic modulus measurements showed no significant change over a period of 34 weeks in degradation conditions (Figure 5c). Results show that there are no significant effects of degradation time on the dynamic compressive modulus ($p = 0.45$). In a pairwise test of spacing on dynamic modulus, all spacings remained significantly different from one another at each time point ($p < 0.005$), confirming that the fiber spacing dependence of the dynamic modulus is maintained up to 34 weeks. Reconstructions from μCT also show little qualitative morphological change in the structure of the scaffolds (Figure 5d). Light regions around the interfaces of the scaffold were observed and may be due to salt deposition from the PBS on the surface of the scaffold. Scaffolds, however showed no structural or mechanical changes over time.

4.5. Comparison of 3D Printed Anatomical IVD Biomechanics to Bovine Lumbar IVDs. Anatomically shaped and sized IVDs were 3D printed using FPLA, and their biomechanical properties under physiologically relevant dynamic testing was performed and compared to the properties of native bovine lumbar IVDs (Figure 6a,b). The mean compressive equilibrium moduli of 3D printed anatomical IVDs (0.94 ± 0.03 MPa) were comparable to the equilibrium modulus of bovine lumbar IVDs (1.01 ± 0.27 MPa, $p = 0.57$, Figure 6c). Mean instantaneous modulus values obtained from the bovine disc were 1.70 ± 0.44 MPa for native IVD, whereas the mean instantaneous modulus obtained from the 3D printed anatomical discs was 1.07 ± 0.03 MPa, which was slightly, but significantly, lower than the native bovine disc ($p = 0.031$).

4.6. Contribution of Alginate to FPLA Biomechanics. To evaluate contribution of a hydrogel to the FPLA scaffold properties, 3D printed scaffolds with and without alginate were tested and compared to alginate alone. Results show no significant difference in the equilibrium (1.36 ± 0.42 MPa, Figure 7a) or instantaneous (2.29 ± 0.76 MPa, Figure 7b) moduli of FPLA+ alginate compared to FPLA scaffold alone (1.60 ± 0.23 MPa, 2.49 ± 0.76 MPa, respectively, $p > 0.05$). Not surprisingly, alginate alone had considerably lower equilibrium (0.05 ± 0.026 MPa) and instantaneous (0.11 ± 0.05 MPa) moduli compared to both groups of 3D printed scaffolds ($p < 0.0001$, Figure 7a,b). Interestingly, the dynamic modulus (determined at 1 Hz) of the FPLA alone (1.48 ± 0.23 MPa) was greater than FPLA+alginate (0.87 ± 0.29 MPa), though this was significantly greater than the dynamic modulus of alginate alone (0.01 ± 0.003 MPa). The phase angle of FPLA+alginate (2.81 ± 0.17°) was significantly lower than FPLA alone (6.53 ± 0.55°, $p < 0.0001$) or alginate alone (7.56 ± 0.24°, $p < 0.0001$, Figure 7c,d). Results from failure testing show that FPLA +alginate has a greater toughness than FPLA alone (87.41 ± 16.55 and 59.76 ± 7.87 kJ/m^3, respectively, $p < 0.05$, Figure 7e)

https://doi.org/10.1021/acsbiomaterials.1c01326
ACS Biomater. Sci. Eng. 2021, 7, 5836−5849

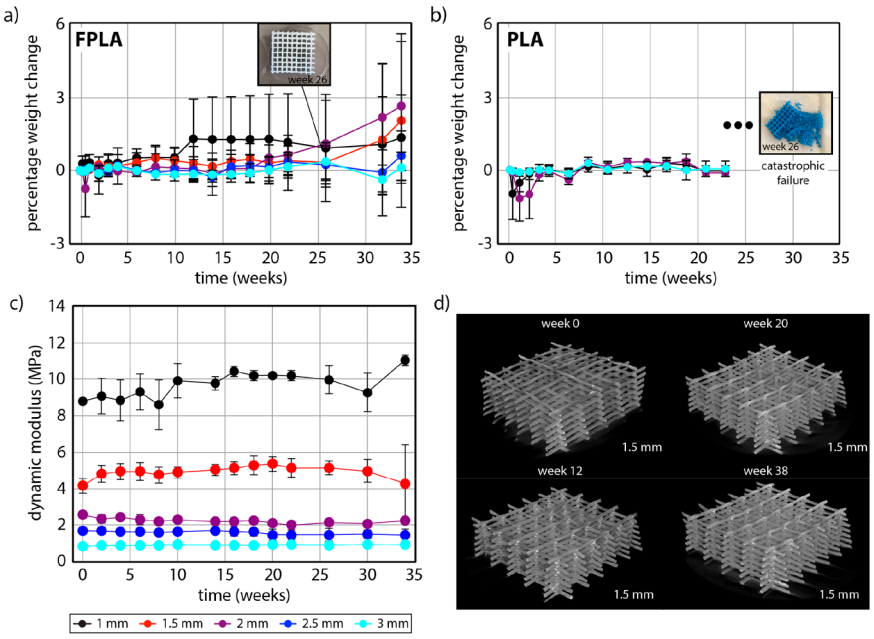

Figure 5. Degradation of FPLA Scaffolds in PBS at 37 °C. (a) Weight change of FPLA scaffolds recorded over 34 weeks in degradation environment. (b) Weight change of PLA scaffolds recorded over 26 weeks in degradation environment. (c) Compressive dynamic modulus of FPLA scaffolds over 34 weeks in degradation environment. (d) μCT reconstructions of 1.5 mm FPLA scaffolds before degradation and after 12, 20, and 38 weeks in degradation environment.

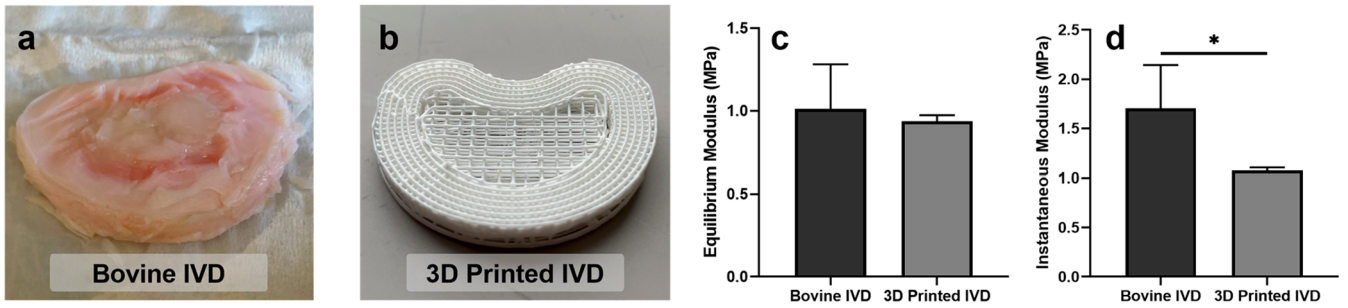

Figure 6. Bovine IVD and 3D printed anatomical IVD mechanics. (a) Bovine lumbar IVD. (b) 3D printed anatomically shaped disc scaffold. (c) Equilibrium modulus of bovine discs and 3D printed disc. (d) Instantaneous modulus of bovine discs and 3D printed disc *p < 0.05.

as well as a greater failure strain (0.78 ± 0.02 and 0.70 ± 0.03, respectively, p < 0.005, Figure 7f).

4.7. Response of NP Cells: 2D Cytotoxicity and 3D Seeding in FPLA/Alginate Composites. FPLA scaffolds did not elicit a cytotoxic effect on NP cells cultured in monolayer for 21 days. At Day 1, control cells and FPLA cultured cells had 98.2 ± 0.1% and 98.3 ± 4.1% viability, respectively. At day 21, control samples had 98.2 ± 0.1% viability and FPLA samples had 98.2 ± 1.3% viability (Figure 8a,b).

To assess the biocompatibility of FPLA scaffold in 3D, NP cells were encapsulated in 1.2% alginate and cast into the pores of 1.5 mm FPLA scaffolds (Figure 1g). This scaffold spacing was selected because it was within the physiological range for both motion segment compression (Figure 3a) and AF tension (Figure 4a). After 2 weeks in culture, NP cells seeded in an FPLA/alginate composite maintained a high level of cell viability when evaluated with fluorescence microscopy, with no major cytotoxic effects observed (Figure 8c). GAG content of the FPLA/alginate composites significantly increased from 0 to 2 weeks in culture (0.16 ± 0.30 to 3.4 ± 1.7 μg/μg, p = 0.0011), and then remained at a similar level after 4 weeks in culture (2.5 ± 1.4 μg/μg, p = 0.0014 between 0 to 4 weeks, p = 0.3 between 2 and 4 weeks, Figure 8d).

H&E staining of the scaffolds exhibited evidence of cell division over the course of the culture duration, where increasing numbers of cell clusters were seen over the 4 weeks in culture (Figure 8e–g). Alcian blue staining showed increased GAG deposition by the cells at 4 weeks in composite culture (Figure 8h–j). GAG deposition was primarily limited to the pericellular environment of the cells with low levels of interterritorial staining observed at 4 weeks in culture.

Biomechanical properties of the engineered scaffolds were tested over time in culture. Results showed that the equilibrium (1.3 ± 0.2 MPa) and dynamic (4.3 ± 0.6 MPa) compressive moduli that were measured at 2 weeks in culture were maintained in scaffolds cultured up to 8 weeks (equilibrium, 1.1 ± 0.2 MPa, p > 0.8 versus 2 weeks; dynamic, 4.4 ± 0.6 MPa; p > 0.5 versus 2 weeks). Phase angle was also similar in scaffolds evaluated after 2 weeks in culture (5.5 ± 0.3°) compared to 8 weeks in culture (5.8 ± 0.1°) (Figure 8k–m).

https://doi.org/10.1021/acsbiomaterials.1c01326
ACS Biomater. Sci. Eng. 2021, 7, 5836–5849

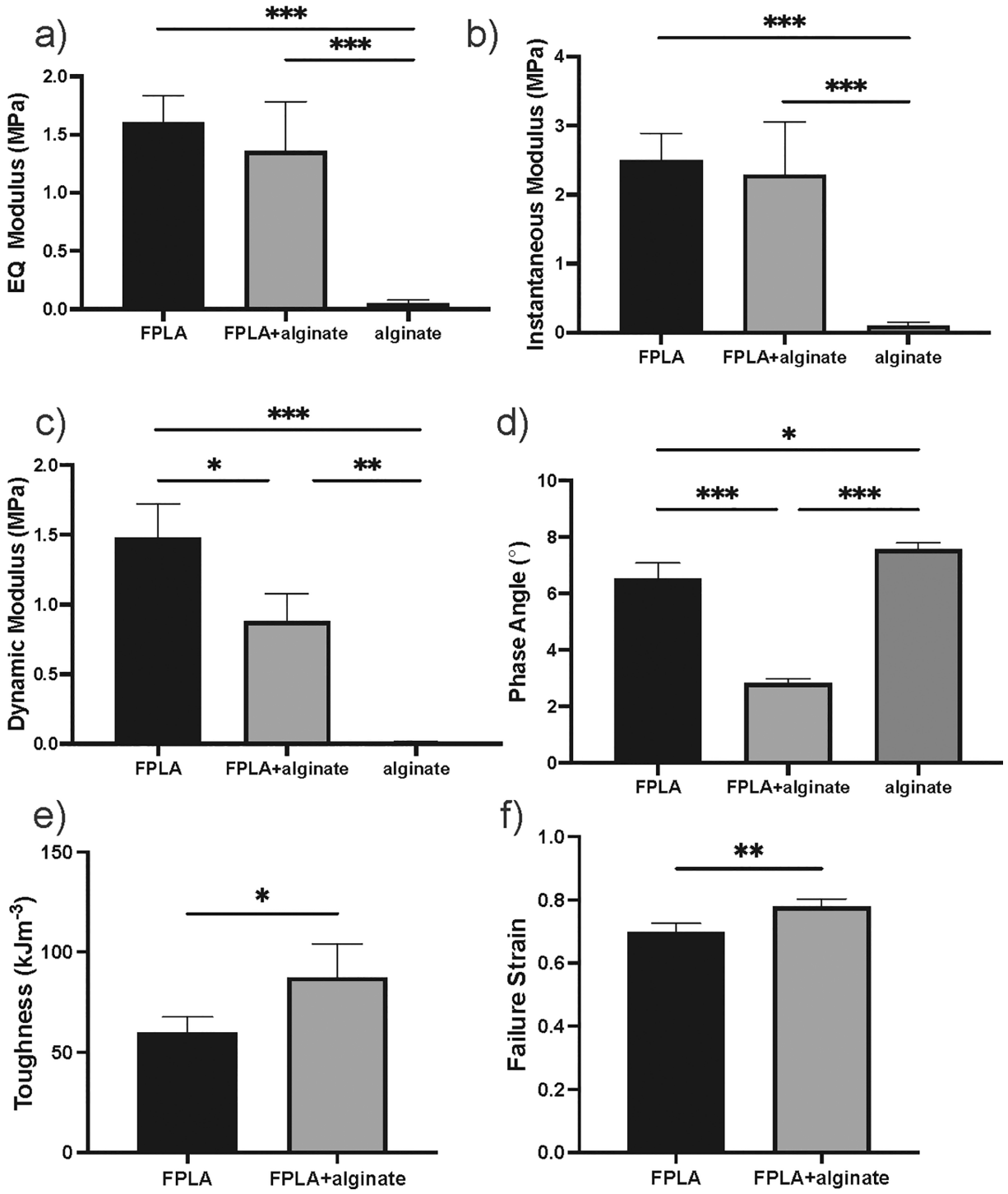

Figure 7. Biomechanics of FPLA+alginate composite. (a) Equilibrium and (b) instantaneous moduli determined from compressive stress relaxation of FPLA alone, FPLA+alginate, or alginate alone. (c) Dynamic modulus and (d) phase angle of samples determined from compressive DMA at 1 Hz frequency. (e) Toughness and (f) failure strain of samples as determined from compressive failure testing. *$p < 0.05$, **$p < 0.005$, ***$p < 0.0005$.

5. DISCUSSION

The goal of this study was to investigate the biomechanical properties of 3D printed FPLA as a tunable mechanical biomimetic scaffold for use as an intervertebral disc scaffold. Specifically, we aim to create FPLA scaffolds that exhibit tensile and compressive properties on the same order of magnitude as native IVD motion segments *de novo* and that are stable, biocompatible, and permissive of ECM deposition. Our results show that 3D printed FPLA scaffolds exhibit a tunable biomimetic compressive modulus that is sensitive to variation in scaffold porosity due to changes in fiber spacing during 3D printing (Figure S1). With a fiber spacing of 1.0 mm, scaffolds exhibited an equilibrium compressive modulus that was within the physiological range for spine motion segments (3−10 MPa).[11] Increasing the spacing between fibers decreased the compressive moduli; however, magnitudes remain within the same order of magnitude as the physiological range. The 3D

https://doi.org/10.1021/acsbiomaterials.1c01326
ACS Biomater. Sci. Eng. 2021, 7, 5836−5849

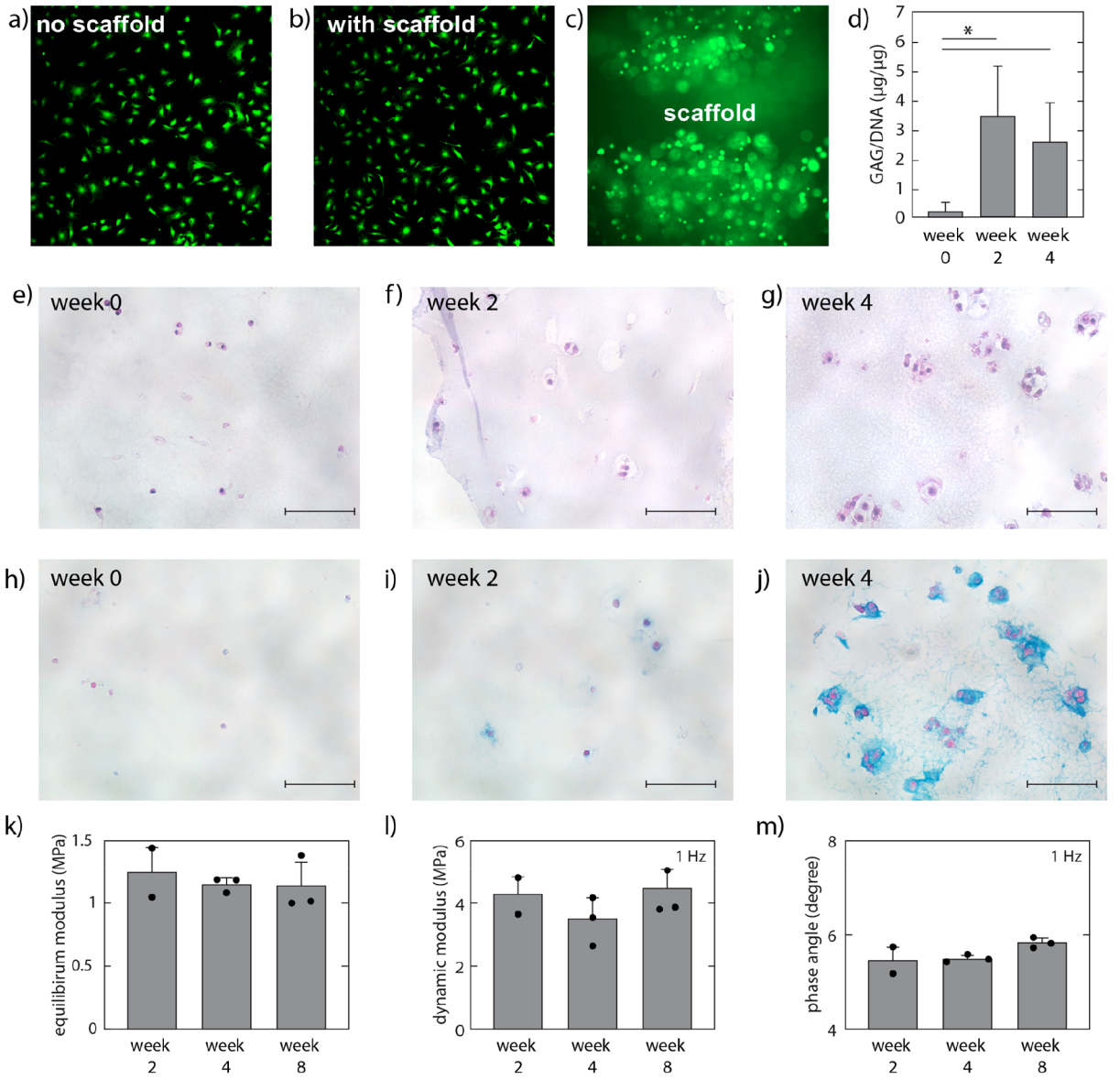

Figure 8. Biological characterization of FPLA scaffolds. Monolayer bovine NP cells cultured (a) without scaffold (control) and (b) with FPLA scaffolds. (c) Live/Dead image of bovine NP cells after 1 week in culture in 1.5 mm FPLA/alginate composite scaffolds. Cells are stained with ethidium homodimer (red-dead) and calcein (green-live). (d) GAG/DNA content of cell-seeded 1.5 mm FPLA/alginate composite scaffolds over 4 weeks in culture. (e−g) H&E staining of cell-seeded 1.5 mm composite scaffolds. (h−j) Alcian blue staining of cell-seeded 1.5 mm composite scaffolds. (k−m) Compressive mechanical properties (k, equilibrium modulus; l, dynamic modulus; m, phase angle) of cell-seeded 1.5 mm composite scaffolds over 8 weeks.

printed FPLA scaffolds also exhibited tunable tensile equilibrium properties (4−15 MPa), which are within the range of multilamellar AF tensile benchmark moduli (10−45 MPa).[21,25] Interestingly, the tensile modulus had a greater dependence on porosity than the compressive modulus with a regression coefficient of −0.538 versus −0.182, respectively (Figure S1). In dynamic testing, both compressive and tensile properties were dependent on fiber spacing, though frequency dependence was more prominent in dynamic tension rather than in compression. Dynamic modulus of FPLA scaffolds in tension ranged from 3 to 10 MPa, which closely matches the range of AF dynamic moduli (1−5 MPa).[26]

The properties of FPLA also exhibited several advantages to standard 3D printed PLA. FPLA properties were closer to the physiological range of IVD tissue mechanics than standard PLA scaffolds, whose compressive equilibrium properties (80 MPa) were an order of magnitude stiffer than the physiological range. Moreover, degradation studies showed virtually no change in the FPLA scaffold mass or compressive mechanical properties up to 34 weeks, demonstrating superior stability of 3D printed FPLA against hydrolysis in comparison to 3D printed PLA, which had brittle failure at 26 weeks.

The IVD exhibits complex mechanical behaviors representative of composite structures and materials. The study of disc mechanics is commonly assessed by measuring material properties of individual anatomical components under controlled loading configurations in compression, tension, and shear that together make up and inform the composite behaviors of

https://doi.org/10.1021/acsbiomaterials.1c01326
ACS Biomater. Sci. Eng. 2021, 7, 5836−5849

the disc. The material properties of the individual disc components are essential to the biomechanics of a composite disc (e.g., Newell et al.[12]). The approach used in this study investigates the tensile and compressive material properties of 3D printed FPLA the same way that native disc tissue components are evaluated mechanically using human cadaveric spines or large animal spines, which exhibit similar properties to human tissue (e.g., bovine lumbar spine). Moreover, we compare the properties of FPLA 3D printed scaffolds to benchmarks established in the literature for disc anatomical tissues tested under the same type of loading configurations. These benchmarks represent the standards in the field against which new disc replacement biomaterials are evaluated. Accordingly, the results show that 3D FPLA meets or exceeds many of these mechanical benchmarks. Of note, there is no preferred fiber orientation in the samples used in the current study. The fiber orientation in our tensile test samples are both along the length of the strip as well perpendicular to the length. Because our samples do not have a preferred fiber orientation, we chose to compare the properties of FPLA strips to bulk AF tensile properties, which are representative of composite multilamellar materials with a heterogeneous fiber direction.

Of the functional properties we evaluated for FPLA samples, the dynamic compressive modulus varied appreciably from that of natural IVD motion segment. The dynamic compressive modulus of IVD motion segments are reported to be ∼30 MPa, whereas FPLA scaffolds exhibited a range of 0.5 to 10 MPa. While FPLA scaffolds were not as stiff in dynamic compression as native motion segment, FPLA properties represent significantly better biomimetic properties than materials that are currently being developed (e.g., hydrogel materials) in the context of IVD tissue engineering or that are used for disc replacement (e.g., titanium cages). Biomedical grade titanium has a modulus on the order of 100 GPa, which is several orders of magnitude higher than the modulus of the native motion segment,[81] which can lead to stress shielding. However, hydrogels used for biomedical applications have moduli in the kPa range,[68] which are orders of magnitude below tissue level and are likely to fail under physiological loading conditions. In the native disc, the apparent dynamic compressive properties are dependent on fluid pressurization within the NP[16] and therefore represent contributions of a solid matrix and an interacting fluid phase. In the absence of a dense hydrated ECM, the dynamic mechanical properties of FPLA are more representative of the flow-independent viscoelastic solid matrix. Interestingly, the phase angle of FPLA scaffold was similar to that of human IVD motion segments tested in dynamic compression (ranging from 5.7 to 9°).[24] Both IVD motion segments and FPLA phase angles are relatively small (i.e., < 10°) indicating that the scaffolds behave predominantly as an elastic structure across all frequencies tested, just as has been observed for human IVDs.[24]

To further demonstrate the utility of 3D printed FPLA, we produced an anatomically biomimetic IVD scaffolds and evaluated their mechanical properties relative to lumbar native disc isolated from bovine spine using a physiologically relevant loading protocol. The anatomical 3D printed IVD was modeled to exhibit dimension similar to bovine IVD, with height of 5.5 mm and a lateral width of 41 mm. The equilibrium modulus was comparable between bovine lumbar IVDs and anatomical 3D printed IVDs (Figure 6), suggesting that the 3D printed anatomical disc mimic the mechanical properties of a bovine IVD in compression and is therefore a promising material for whole disc scaffolding. While the equilibrium modulus of the 3D printed anatomical discs were remarkably similar to native IVD samples under unconfined compression, the observed lower instantaneous moduli suggest that fluid pressurization in native IVD remains higher than porous 3D printed scaffolds with biomimetic equilibrium mechanical properties. Future efforts will explore engineering approaches to for enhance fluid pressurization of 3D printed FPLA scaffolds.

One possible approach for enhancing pressurization of the porous scaffold is to incorporate a hydrogel into a composite. In FPLA+alginate structures, the equilibrium and instantaneous modulus of FPLA with and without alginate were comparable and were significantly greater than alginate alone. This suggests that under subfailure strains (up to 25%) the alginate does not pull away from the FPLA, yet it does not offer significant contribution to scaffold stiffness. Under physiological dynamic loading, interactions between FPLA and alginate resulted in slightly lower dynamic modulus than FPLA alone. The composite also exhibited a lower phase angle than either component alone, demonstrating that interactions between the two polymer systems led to less energy dissipation. Moreover, our results show that FPLA+alginate has a significantly greater toughness and failure strain compared to FPLA alone. These findings suggest that in some conditions, the FPLA+alginate composite has enhanced mechanical function compared to FPLA alone, which may be further optimized with use of other hydrogels designed to withstand IVD stress and strains.

The mechanical characterization of cell-seeded FPLA composite scaffolds over 8 weeks in culture also showed no significant changes in the equilibrium modulus, dynamic modulus, and phase angle, demonstrating the stability of these scaffolds in cell culture. Not surprisingly, the addition of cell-deposited ECM did not induce further increases in the mechanical properties because the contributions of cell-deposited ECM are small (likely in kPa range) compared to the *de novo* properties of the FPLA (shown here to be in MPa range). The compressive equilibrium mechanical properties of the FPLA scaffolds are superior to prior tissue engineered whole disc replacements which typically have a compressive equilibrium modulus on the order of 50 kPa at the end of culture, a level below the target physiological range.[37,55] Indeed, additional maturation for 10 to 20 weeks *in vivo* was needed in one study to reach native equilibrium properties.[53]

While cell seeding of FPLA is not necessary for creating mechanically strong constructs for implantation, the addition of cells may aid in the deposition of a native ECM and in the integration of the scaffolds to the surrounding tissues. Importantly, no cytotoxic effects were observed for NP cell 2D monolayer culture or in the 3D composite cultures. Moreover, both histological staining (alcian blue) and GAG production assays showed that there is an increase in GAG deposition over time, however this was not necessary for maintenance of mechanical integrity of the scaffold in culture. The histological observations of the current study are consistent with prior studies; Nerurkar et al. and Nesti et al. both observed increased proteoglycan staining in their respective hydrogel-based whole disc constructs over a period of weeks in culture with patterns of pericellular proteoglycan staining.[37,82] We observed an initial increase in GAG content followed by maintenance at the 4 week time point. It is important to note that overall DNA content was also increasing over time, though the GAG content appeared to plateau compared to DNA content. While most whole disc replacement studies observe a steady increase in GAG production[37,55,82−84] *in vitro*, some

https://doi.org/10.1021/acsbiomaterials.1c01326
ACS Biomater. Sci. Eng. 2021, 7, 5836−5849

observe decreases in GAG content that could be attributed to degradation of the alginate.[85,86]

We choose NP cells for biocompatibility as a representative differentiated IVD cell; however, biocompatibility is expected to be the same for both AF and NP cells on the FPLA material. With regard to matrix production, NP cells were chosen for their ability to deposit proteoglycan rich matrix. Cells were seeded in a hydrogel in 3D as opposed to directly on the scaffold to avoid cell elongation on the fibers and potential dedifferentiation of NP cells. To further evaluate the potential of FPLA for fibrocartilaginous differentiation, we investigated the response of bone marrow derived mesenchymal stem cells (MSCs) to seeding on FPLA alone or FPLA+alginate up to day 7 in culture (Figure S2). MSCs cultured on FPLA were viable and the scaffold promoted a fibrocartilaginous phenotype in MSC laden constructs with robust expression of COL1A, COL2A, and ACAN, mirroring the expression of native AF.

The use of 3D printed FPLA scaffolds offers an alternative "off the shelf" scaffold for tissue engineering or implantion; FPLA scaffolds exhibit biomimetic properties of the spine motion segment *de novo* without the addition of cells. FPLA is also a high-melting temperature material, that is printed at 240 °C and melts at 180 °C; therefore, it can be sterilized in an autoclave at 121 °C (250 °F) and dried at 132 °C (270 °F) like traditional surgical materials. Additionally, 3D printing has the potential for customized scaffolds to meet patient spinal anatomy, such as disc height, volume, and ratio of NP to AF cross sectional area. Indeed, personalized 3D printed metal implants have been shown to reduce the risk of implant failure by ensuring improved matching with the patient vertebrae dimension and morphology.[87] Future studies will investigate the use of 3D printing for tuning of shape, size, and integration components into animal spines *in vivo*.

Our findings of biomimetic tensile and compressive, equilibrium, and dynamic properties of 3D printed FPLA demonstrate its potential in disc replacement applications. This study is the first step toward an anatomical 3D printed disc replacement. But many additional questions remain, and some limitations exist. One limitation is that this study did not evaluate the torsional properties of 3D printed FPLA. Shear due to bending or rotation causes very high stresses at the disc interfaces that may also create high stresses between the FPLA–alginate interfaces that would be important to consider. Future studies will also evaluate the response of scaffold composites to fatigue loading. These studies were performed with NP cells (as a representative IVD differentiated cell type) and MSCs for assessing short-term gene expression changes. Future studies should evaluate either a combination of NP and AF cells for regional responses on 3D FPLA and/or MSCs in long-term culture for translational potential into an *in vivo* model. The cell density used within the scaffolds was lower than that of native IVD, which was in part restricted by the number of cells acquired from fresh bovine IVD isolation. The expectation is that with increased cell density, greater ECM deposition within the construct may provide additional dynamic contributions to matrix pressurization, although some studies suggest that nutrient limitations with very high cell seeding density may occur in cell-seeded hydrogels.[88] However, since these scaffolds have *de novo* mechanical properties without the need for ECM deposition, the addition of cells may be beneficial for integration or molecular signaling with surrounding tissue but is not required for maintaining mechanical function. Although the primary mechanism of PLA degradation is hydrolysis of the ester-bond backbone, future studies may evaluate degradation under loading or *in vivo* conditions.[76]

6. CONCLUSIONS

This study demonstrates the novelty and versatility of flexible 3D printed FPLA in generating tunable viscoelastic scaffolds that mimic the native mechanical properties of human intervertebral disc motion segments. These scaffolds were also stable and biocompatible and are permissive of both fibrocartilaginous matrix expression by MSCs and proteoglycan rich extracellular matrix deposition by NP cells.

■ ASSOCIATED CONTENT

Supporting Information

The Supporting Information is available free of charge at https://pubs.acs.org/doi/10.1021/acsbiomaterials.1c01326.

Graphs of relationship between compressive or tensile moduli and porosity of FPLA scaffolds, Live/Dead imaging, SEM, cell count, and ECM gene expression of MSCs seeded on FPLA and FPLA+Alginate scaffolds (PDF)

■ AUTHOR INFORMATION

Corresponding Author

Nadeen O. Chahine − *Department of Orthopedic Surgery and Department of Biomedical Engineering, Columbia University, New York, New York 10031, United States;* orcid.org/0000-0002-0478-6042; Phone: 212-305-1515; Email: noc7@columbia.edu; Fax: 212-305-2741

Authors

Samantha L. Marshall − *Department of Orthopedic Surgery, Columbia University, New York, New York 10031, United States*

Timothy D. Jacobsen − *Department of Orthopedic Surgery and Department of Biomedical Engineering, Columbia University, New York, New York 10031, United States*

Erik Emsbo − *Department of Biomedical Engineering, Columbia University, New York, New York 10031, United States*

Archana Murali − *Department of Biomedical Engineering, Columbia University, New York, New York 10031, United States*

Kevin Anton − *Department of Biomedical Engineering, Columbia University, New York, New York 10031, United States*

Jessica Z. Liu − *Department of Biomedical Engineering, Columbia University, New York, New York 10031, United States*

Helen H. Lu − *Department of Biomedical Engineering, Columbia University, New York, New York 10031, United States*

Complete contact information is available at: https://pubs.acs.org/10.1021/acsbiomaterials.1c01326

Author Contributions

S.M. contributed to the methodology, investigation, writing - original draft, writing - review and editing, and visualization. T.J. contributed to the methodology, investigation, writing: review and editing. E.E. contributed to the resources and investigation. A.M. contributed to the resources and investigation. K.A. contributed to the resources and investigation. J.L. contributed

https://doi.org/10.1021/acsbiomaterials.1c01326
ACS Biomater. Sci. Eng. 2021, 7, 5836−5849

to the resources and investigation. H.L. contributed to the methodology, investigation, supervision, and writing - review and editing, N.C. contributed to the conceptualization, methodology, writing - review and editing, supervision, project administration, and funding acquisition.

Notes

The authors declare no competing financial interest.

■ ACKNOWLEDGMENTS

The authors would like to thank Jacob Rigos for assistance with preliminary tests. The authors would also like to acknowledge the CUIMC HICCC Confocal and Specialized Microscopy Shared Resource (CSMSR). This study was supported in part by NIH R01 AR069668, R01 AR077760, R21 AR080516, P30 CA013696 (microscopy core), and by institutional support from Columbia University.

■ REFERENCES

(1) Serra, T.; Capelli, C.; Toumpaniari, R.; Orriss, I. R.; Leong, J. J. H.; Dalgarno, K.; Kalaskar, D. M. Design and Fabrication of 3D-Printed Anatomically Shaped Lumbar Cage for Intervertebral Disc (IVD) Degeneration Treatment. *Biofabrication* **2016**, *8* (3), 035001.

(2) Adams, M. A. Biomechanics of Back Pain. *Acupunct. Med.* **2004**, *22* (4), 178−188.

(3) Bogduk, N. The Lumbar Disc and Low Back Pain. *Neurosurg. Clin. N. Am.* **1991**, *2* (4), 791−806.

(4) Urban, J. P. G.; Roberts, S. Degeneration of the Intervertebral Disc. *Arthritis Res. Ther.* **2003**, *5* (3), 120−130.

(5) Melrose, J.; Ghosh, P.; Taylor, T. K. F. A Comparative Analysis of the Differential Spatial and Temporal Distributions of the Large (Aggrecan, Versican) and Small (Decorin, Biglycan, Fibromodulin) Proteoglycans of the Intervertebral Disc. *J. Anat.* **2001**, *198* (1), 3−15.

(6) Adams, M. A.; McNally, D. S.; Dolan, P. Stress" Distributions inside Intervertebral Discs. *J. Bone Jt. Surg., Br. Vol.* **1996**, *78* (6), 965−972.

(7) Rider, S. M.; Mizuno, S.; Kang, J. D. Molecular Mechanisms of Intervertebral Disc Degeneration. *Spine Surg. Relat. Res.* **2019**, *3* (1), 1−11.

(8) Lotz, J. C.; Ulrich, J. A. Innervation, Inflammation, and Hypermobility May Characterize Pathologic Disc Degeneration: Review of Animal Model Data. *J. Bone Jt. Surg.* **2006**, *88*, 76.

(9) An, H. S.; Masuda, K.; Inoue, N. Intervertebral Disc Degeneration: Biological Biomechanical Factors. *J. Orthop. Sci.* **2006**, *11* (5), 541−552.

(10) Iatridis, J. C.; Setton, L. A.; Weidenbaum, M.; Mow, V. C. Alterations in the Mechanical Behavior of the Human Lumbar Nucleus Pulposus with Degeneration and Aging. *J. Orthop. Res.* **1997**, *15* (2), 318−322.

(11) Nerurkar, N. L.; Elliott, D. M.; Mauck, R. L. Mechanical Design Criteria for Intervertebral Disc Tissue Engineering. *J. Biomech.* **2010**, *43* (6), 1017−1030.

(12) Newell, N.; Little, J. P.; Christou, A.; Adams, M. A.; Adam, C. J.; Masouros, S. D. Biomechanics of the Human Intervertebral Disc: A Review of Testing Techniques and Results. *J. Mech. Behav. Biomed. Mater.* **2017**, *69*, 420−434.

(13) Berkson, M. H.; Nachemson, A.; Schultz, A. B. Mechanical Properties of Human Lumbar Spine Lotion Segments— Part II: Responses in Compression and Shear; Influence of Gross Morphology. *J. Biomech. Eng.* **1979**, *101* (1), 53−57.

(14) Adams, M. A.; Roughley, P. J. What Is Intervertebral Disc Degeneration, and What Causes It? *Spine (Philadelphia)* **2006**, *31* (18), 2151−2161.

(15) Gardner-Morse, M. G.; Stokes, I. A. F. Structural Behavior of Human Lumbar Spinal Motion Segments. *J. Biomech.* **2004**, *37* (2), 205−212.

(16) Iatridis, J. C.; Weidenbaum, M.; Setton, L. A.; Mow, V. C. Is the Nucleus Pulposus a Solid or a Fluid? Mechanical Behaviors of the Nucleus Pulposus of the Human Intervertebral Disc. *Spine (Philadelphia)* **1996**, *21* (10), 1174−1184.

(17) Nachemson, A. L.; Schultz, A. B.; Berkson, M. H. Mechanical Properties of Human Lumbar Spine Motion Segments. *Spine (Philadelphia)* **1979**, *4* (1), 1−8.

(18) Urban, J. P. G.; Maroudas, A. Swelling of the Intervertebral Disc in Vitro. *Connect. Tissue Res.* **1981**, *9* (1), 1−10.

(19) Eyre, D. R.; Muir, H. Types I and II Collagens in Intervertebral Disc. Interchanging Radial Distributions in Annulus Fibrosus. *Biochem. J.* **1976**, *157* (1), 267−270.

(20) Tsantrizos, A.; Ito, K.; Aebi, M.; Steffen, T. Internal Strains in Healthy and Degenerated Lumbar Intervertebral Discs. *Spine (Philadelphia)* **2005**, *30* (19), 2129−2137.

(21) Kasra, M.; Parnianpour, M.; Shirazi-Adl, A.; Wang, J. L.; Grynpas, M. D. Effect of Strain Rate on Tensile Properties of Sheep Disc Anulus Fibrosus. *Technol. Heal. Care* **2004**, *12* (4), 333−342.

(22) Iatridis, J. C.; Mente, P. L.; Stokes, I. A. F.; Aronsson, D. D.; Alini, M. Compression-Induced Changes in Intervertebral Disc Properties in a Rat Tail Model. *Spine (Philadelphia)* **1999**, *24* (10), 996−1002.

(23) Amin, D. B.; Lawless, I. M.; Sommerfeld, D.; Stanley, R. M.; Ding, B.; Costi, J. J. The Effect of Six Degree of Freedom Loading Sequence on the In-Vitro Compressive Properties of Human Lumbar Spine Segments. *J. Biomech.* **2016**, *49* (14), 3407−3414.

(24) Costi, J. J.; Stokes, I. A.; Gardner-Morse, M. G.; Iatridis, J. C. Frequency-Dependent Behavior of the Intervertebral Disc in Response to Each of Six Degree of Freedom Dynamic Loading. *Spine (Philadelphia)* **2008**, *33* (16), 1731−1738.

(25) Ebara, S.; Iatridis, J. C.; Setton, L. A.; Foster, R. J.; Mow, V. C.; Weidenbaum, M. Tensile Properties of Nondegenerate Human Lumbar Anulus Fibrosus. *Spine (Philadelphia)* **1996**, *21* (4), 452−461.

(26) Sen, S.; Jacobs, N. T.; Boxberger, J. I.; Elliott, D. M. Human Annulus Fibrosus Dynamic Tensile Modulus Increases with Degeneration. *Mech. Mater.* **2012**, *44*, 93−98.

(27) Boucher, H. H. A METHOD OF SPINAL FUSION. *J. Bone Jt. Surg., Br. Vol.* **1959**, *41-B* (2), 248−259.

(28) Phillips, F. M.; Slosar, P. J.; Youssef, J. A.; Andersson, G.; Papatheofanis, F. Lumbar Spine Fusion for Chronic Low Back Pain Due to Degenerative Disc Disease. *Spine (Philadelphia)* **2013**, *38* (7), E409−E422.

(29) Freeman, B. J. C.; Davenport, J. Total Disc Replacement in the Lumbar Spine: A Systematic Review of the Literature. *Eur. Spine J.* **2006**, *15* (S3), 439−447.

(30) Martin, B. I.; Mirza, S. K.; Comstock, B. A.; Gray, D. T.; Kreuter, W.; Deyo, R. A. Reoperation Rates Following Lumbar Spine Surgery and the Influence of Spinal Fusion Procedures. *Spine (Philadelphia)* **2007**, *32* (3), 382−387.

(31) Turner, J. A; Ersek, M.; Herron, L.; Haselkorn, J.; Kent, D.; Ciol, M. A; Deyo, R. Patient outcomes after lumbar spinal fusions. *JAMA* **1992**, *268* (7), 907−911.

(32) Park, P.; Garton, H. J.; Gala, V. C.; Hoff, J. T.; McGillicuddy, J. E. Adjacent Segment Disease after Lumbar or Lumbosacral Fusion: Review of the Literature. *Spine (Philadelphia)* **2004**, *29* (17), 1938−1944.

(33) Hilibrand, A. S.; Carlson, G. D.; Palumbo, M. A.; Jones, P. K.; Bohlman, H. H. Radiculopathy and Myelopathy at Segments Adjacent to the Site of a Previous Anterior Cervical Arthrodesis. *J. Bone Jt. Surg. - Ser. A* **1999**, *81* (4), 519−528.

(34) Nunley, P. D.; Jawahar, A.; Kerr, E. J.; Gordon, C. J.; Cavanaugh, D. A.; Birdsong, E. M.; Stocks, M.; Danielson, G. Factors Affecting the Incidence of Symptomatic Adjacent-Level Disease in Cervical Spine after Total Disc Arthroplasty: 2- to 4-Year Follow-up of 3 Prospective Randomized Trials. *Spine (Philadelphia)* **2012**, *37* (6), 445−451.

(35) Delamarter, R. B.; Zigler, J. Five-Year Reoperation Rates, Cervical Total Disc Replacement versus Fusion, Results of a Prospective Randomized Clinical Trial. *Spine (Philadelphia)* **2013**, *38* (9), 711−717.

(36) Lee, C. S.; Hwang, C. J.; Lee, S.-W.; Ahn, Y.-J.; Kim, Y.-T.; Lee, D.-H.; Lee, M. Y. Risk Factors for Adjacent Segment Disease after Lumbar Fusion. *Eur. Spine J.* **2009**, *18* (11), 1637−1643.

https://doi.org/10.1021/acsbiomaterials.1c01326
ACS Biomater. Sci. Eng. 2021, 7, 5836−5849

(37) Nerurkar, N. L.; Sen, S.; Huang, A. H.; Elliott, D. M.; Mauck, R. L. Engineered Disc-Like Angle-Ply Structures for Intervertebral Disc Replacement. *Spine (Philadelphia)* **2010**, *35* (8), 867−873.
(38) Baer, A. E.; Wang, J. Y.; Kraus, V. B.; Setton, L. A. Collagen Gene Expression and Mechanical Properties of Intervertebral Disc Cell−Alginate Cultures. *J. Orthop. Res.* **2001**, *19* (1), 2−10.
(39) Chou, A. I.; Nicoll, S. B. Characterization of Photocrosslinked Alginate Hydrogels for Nucleus Pulposus Cell Encapsulation. *J. Biomed. Mater. Res., Part A* **2009**, *91A* (1), 187−194.
(40) Malhotra, N. R.; Han, W. M.; Beckstein, J.; Cloyd, J.; Chen, W.; Elliott, D. M. An Injectable Nucleus Pulposus Implant Restores Compressive Range of Motion in the Ovine Disc. *Spine (Philadelphia)* **2012**, *37* (18), E1099−E1105.
(41) Omlor, G. W.; Nerlich, A. G.; Lorenz, H.; Bruckner, T.; Richter, W.; Pfeiffer, M.; Gühring, T. Injection of a Polymerized Hyaluronic Acid/Collagen Hydrogel Matrix in an in Vivo Porcine Disc Degeneration Model. *Eur. Spine J.* **2012**, *21* (9), 1700−1708.
(42) Cloyd, J. M.; Malhotra, N. R.; Weng, L.; Chen, W.; Mauck, R. L.; Elliott, D. M. Material Properties in Unconfined Compression of Human Nucleus Pulposus, Injectable Hyaluronic Acid-Based Hydrogels and Tissue Engineering Scaffolds. *Eur. Spine J.* **2007**, *16* (11), 1892−1898.
(43) Gloria, A.; Borzacchiello, A.; Causa, F.; Ambrosio, L. Rheological Characterization of Hyaluronic Acid Derivatives as Injectable Materials toward Nucleus Pulposus Regeneration. *J. Biomater. Appl.* **2012**, *26* (6), 745−759.
(44) Su, W. Y.; Chen, Y. C.; Lin, F. H. Injectable Oxidized Hyaluronic Acid/Adipic Acid Dihydrazide Hydrogel for Nucleus Pulposus Regeneration. *Acta Biomater.* **2010**, *6* (8), 3044−3055.
(45) Nerurkar, N. L.; Mauck, R. L.; Elliott, D. M. ISSLS Prize Winner: Integrating Theoretical and Experimental Methods for Functional Tissue Engineering of the Annulus Fibrosus. *Spine (Philadelphia)* **2008**, *33* (25), 2691−2701.
(46) Nerurkar, N. L.; Baker, B. M.; Sen, S.; Wible, E. E.; Elliott, D. M.; Mauck, R. L. Nanofibrous Biologic Laminates Replicate the Form and Function of the Annulus Fibrosus. *Nat. Mater.* **2009**, *8* (12), 986−992.
(47) Martin, J. T.; Milby, A. H.; Chiaro, J. A.; Kim, D. H.; Hebela, N. M.; Smith, L. J.; Elliott, D. M.; Mauck, R. L. Translation of an Engineered Nanofibrous Disc-like Angle-Ply Structure for Intervertebral Disc Replacement in a Small Animal Model. *Acta Biomater.* **2014**, *10* (6), 2473−2481.
(48) Wismer, N.; Grad, S.; Fortunato, G.; Ferguson, S. J.; Alini, M.; Eglin, D. Biodegradable Electrospun Scaffolds for Annulus Fibrosus Tissue Engineering: Effect of Scaffold Structure and Composition on Annulus Fibrosus Cells in Vitro. *Tissue Eng., Part A* **2014**, *20* (3−4), 140123085256009.
(49) Chik, T. K.; Ma, X. Y.; Choy, T. H.; Li, Y. Y.; Diao, H. J.; Teng, W. K.; Han, S. J.; Cheung, K. M. C.; Chan, B. P. Photochemically Crosslinked Collagen Annulus Plug: A Potential Solution Solving the Leakage Problem of Cell-Based Therapies for Disc Degeneration. *Acta Biomater.* **2013**, *9* (9), 8128−8139.
(50) Borde, B.; Grunert, P.; Härtl, R.; Bonassar, L. J. Injectable, High-Density Collagen Gels for Annulus Fibrosus Repair: An in Vitro Rat Tail Model. *J. Biomed. Mater. Res., Part A* **2015**, *103* (8), 2571−2581.
(51) Bao, J.; Lv, W.; Sun, Y.; Deng, Y. Electrospun Antimicrobial Microfibrous Scaffold for Annulus Fibrosus Tissue Engineering. *J. Mater. Sci.* **2013**, *48* (12), 4223−4232.
(52) Grunert, P.; Borde, B. H.; Hudson, K. D.; MacIelak, M. R.; Bonassar, L. J.; Härtl, R. Annular Repair Using High-Density Collagen Gel: A Rat-Tail in Vivo Model. *Spine (Philadelphia)* **2014**, *39* (3), 198−206.
(53) Gullbrand, S. E.; Ashinsky, B. G.; Bonnevie, E. D.; Kim, D. H.; Engiles, J. B.; Smith, L. J.; Elliott, D. M.; Schaer, T. P.; Smith, H. E.; Mauck, R. L. Long-Term Mechanical Function and Integration of an Implanted Tissue-Engineered Intervertebral Disc. *Sci. Transl. Med.* **2018**, *10* (468), eaau0670.
(54) Mizuno, H.; Roy, A. K.; Vacanti, C. A.; Kojima, K.; Ueda, M.; Bonassar, L. J. Tissue-Engineered Composites of Anulus Fibrosus and Nucleus Pulposus for Intervertebral Disc Replacement. *Spine (Philadelphia)* **2004**, *29* (12), 1290−1297.
(55) Mizuno, H.; Roy, A. K.; Zaporojan, V.; Vacanti, C. A.; Ueda, M.; Bonassar, L. J. Biomechanical and Biochemical Characterization of Composite Tissue-Engineered Intervertebral Discs. *Biomaterials* **2006**, *27* (3), 362−370.
(56) Bowles, R. D.; Gebhard, H. H.; Härtl, R.; Bonassar, L. J. Tissue-Engineered Intervertebral Discs Produce New Matrix, Maintain Disc Height, and Restore Biomechanical Function to the Rodent Spine. *Proc. Natl. Acad. Sci. U. S. A.* **2011**, *108* (32), 13106−13111.
(57) Lazebnik, M.; Singh, M.; Glatt, P.; Friis, L. A.; Berkland, C. J.; Detamore, M. S. Biomimetic Method for Combining the Nucleus Pulposus and Annulus Fibrosus for Intervertebral Disc Tissue Engineering. *J. Tissue Eng. Regener. Med.* **2011**, *5* (8), e179−e187.
(58) Xu, B.; Xu, H.; Wu, Y.; Li, X.; Zhang, Y.; Ma, X.; Yang, Q. Intervertebral Disc Tissue Engineering with Natural Extracellular Matrix-Derived Biphasic Composite Scaffolds. *PLoS One* **2015**, *10* (4), e0124774.
(59) Martin, J. T.; Milby, A. H.; Ikuta, K.; Poudel, S.; Pfeifer, C. G.; Elliott, D. M.; Smith, H. E.; Mauck, R. L. A Radiopaque Electrospun Scaffold for Engineering Fibrous Musculoskeletal Tissues: Scaffold Characterization and in Vivo Applications. *Acta Biomater.* **2015**, *26*, 97−104.
(60) Iu, J.; Santerre, J. P.; Kandel, R. A. Towards Engineering Distinct Multi-Lamellated Outer and Inner Annulus Fibrosus Tissues. *J. Orthop. Res.* **2018**, *36* (5), 1346−1355.
(61) Iu, J.; Massicotte, E.; Li, S.; Hurtig, M. B.; Toyserkani, E.; Santerre, J. P.; Kandel, R. A. In Vitro Generated Intervertebral Discs: Toward Engineering Tissue Integration. *Tissue Eng., Part A* **2017**, *23* (17−18), 1001−1010.
(62) Moriguchi, Y.; Mojica-Santiago, J.; Grunert, P.; Pennicooke, B.; Berlin, C.; Khair, T.; Navarro-Ramirez, R.; Ricart Arbona, R. J.; Nguyen, J.; Härtl, R.; Bonassar, L. J. Total Disc Replacement Using Tissue-Engineered Intervertebral Discs in the Canine Cervical Spine. *PLoS One* **2017**, *12* (10), e0185716.
(63) Martin, J. T.; Gullbrand, S. E.; Mohanraj, B.; Ashinsky, B. G.; Kim, D. H.; Ikuta, K.; Elliott, D. M.; Smith, L. J.; Mauck, R. L.; Smith, H. E. Optimization of Preculture Conditions to Maximize the In Vivo Performance of Cell-Seeded Engineered Intervertebral Discs. *Tissue Eng., Part A* **2017**, *23* (17−18), 923−934.
(64) Martin, J. T.; Kim, D. H.; Milby, A. H.; Pfeifer, C. G.; Smith, L. J.; Elliott, D. M.; Smith, H. E.; Mauck, R. L. In Vivo Performance of an Acellular Disc-like Angle Ply Structure (DAPS) for Total Disc Replacement in a Small Animal Model. *J. Orthop. Res.* **2017**, *35* (1), 23−31.
(65) Rosenzweig, D.; Carelli, E.; Steffen, T.; Jarzem, P.; Haglund, L. 3D-Printed ABS and PLA Scaffolds for Cartilage and Nucleus Pulposus Tissue Regeneration. *Int. J. Mol. Sci.* **2015**, *16* (12), 15118−15135.
(66) Liang, X.; Gao, J.; Xu, W.; Wang, X.; Shen, Y.; Tang, J.; Cui, S.; Yang, X.; Liu, Q.; Yu, L.; Ding, J. Structural Mechanics of 3D-Printed Poly(Lactic Acid) Scaffolds with Tetragonal, Hexagonal and Wheel-like Designs. *Biofabrication* **2019**, *11* (3), 035009.
(67) van Uden, S.; Silva-Correia, J.; Correlo, V. M.; Oliveira, J. M.; Reis, R. L. Custom-Tailored Tissue Engineered Polycaprolactone Scaffolds for Total Disc Replacement. *Biofabrication* **2015**, *7* (1), 015008.
(68) Oyen, M. L. Mechanical Characterisation of Hydrogel Materials. *Int. Mater. Rev.* **2014**, *59* (1), 44−59.
(69) Whatley, B. R.; Kuo, J.; Shuai, C.; Damon, B. J.; Wen, X. Fabrication of a Biomimetic Elastic Intervertebral Disk Scaffold Using Additive Manufacturing. *Biofabrication* **2011**, *3* (1), 015004.
(70) Busscher, I.; Ploegmakers, J. J. W.; Verkerke, G. J.; Veldhuizen, A. G. Comparative Anatomical Dimensions of the Complete Human and Porcine Spine. *Eur. Spine J.* **2010**, *19* (7), 1104−1114.
(71) Choi, S. H.; Lee, H.; Cho, J. H.; Jung, J. Il; Lee, D.-H. Radiological Parameters of Undegenerated Cervical Vertebral Segments in a Korean Population. *Clin. Orthop. Surg.* **2017**, *9* (1), 63.

https://doi.org/10.1021/acsbiomaterials.1c01326
ACS Biomater. Sci. Eng. 2021, 7, 5836−5849

(72) Kim, G. H. Electrospun PCL Nanofibers with Anisotropic Mechanical Properties as a Biomedical Scaffold. *Biomed. Mater.* **2008**, *3* (2), 025010.
(73) Li, W.-J.; Mauck, R. L.; Cooper, J. A.; Yuan, X.; Tuan, R. S. Engineering Controllable Anisotropy in Electrospun Biodegradable Nanofibrous Scaffolds for Musculoskeletal Tissue Engineering. *J. Biomech.* **2007**, *40* (8), 1686−1693.
(74) Hutmacher, D. W.; Schantz, T.; Zein, I.; Ng, K. W.; Teoh, S. H.; Tan, K. C. Mechanical Properties and Cell Cultural Response of Polycaprolactone Scaffolds Designed and Fabricated via Fused Deposition Modeling. *J. Biomed. Mater. Res.* **2001**, *55* (2), 203−216.
(75) Fulcher, G. R.; Hukins, D. W. L.; Shepherd, D. E. T. Viscoelastic Properties of Bovine Articular Cartilage Attached to Subchondral Bone at High Frequencies. *BMC Musculoskeletal Disord.* **2009**, *10* (1), 1−7.
(76) da Silva, D.; Kaduri, M.; Poley, M.; Adir, O.; Krinsky, N.; Shainsky-Roitman, J.; Schroeder, A. Biocompatibility, Biodegradation and Excretion of Polylactic Acid (PLA) in Medical Implants and Theranostic Systems. *Chem. Eng. J.* **2018**, *340*, 9−14.
(77) Vergroesen, P.-P. A.; van der Veen, A. J.; van Royen, B. J.; Kingma, I.; Smit, T. H. Intradiscal Pressure Depends on Recent Loading and Correlates with Disc Height and Compressive Stiffness. *Eur. Spine J.* **2014**, *23* (11), 2359−2368.
(78) Mauck, R. L.; Yuan, X.; Tuan, R. S. Chondrogenic Differentiation and Functional Maturation of Bovine Mesenchymal Stem Cells in Long-Term Agarose Culture. *Osteoarthr. Cartil.* **2006**, *14* (2), 179−189.
(79) Enobakhare, B. O.; Bader, D. L.; Lee, D. A. Quantification of Sulfated Glycosaminoglycans in Chondrocyte/Alginate Cultures, by Use of 1,9-Dimethylmethylene Blue. *Anal. Biochem.* **1996**, *243* (1), 189−191.
(80) Zheng, C.; Levenston, M. Fact versus Artifact: Avoiding Erroneous Estimates of Sulfated Glycosaminoglycan Content Using the Dimethylmethylene Blue Colorimetric Assay for Tissue-Engineered Constructs. *Eur. Cells Mater.* **2015**, *29* (1), 224−236.
(81) Niinomi, M. Mechanical Properties of Biomedical Titanium Alloys. *Mater. Sci. Eng., A* **1998**, *243* (1−2), 231−236.
(82) Nesti, L. J.; Li, W.-J. J.; Shanti, R. M.; Jiang, Y. J.; Jackson, W.; Freedman, B. A.; Kuklo, T. R.; Giuliani, J. R.; Tuan, R. S. Intervertebral Disc Tissue Engineering Using a Novel Hyaluronic Acid-Nanofibrous Scaffold (HANFS) Amalgam. *Tissue Eng., Part A* **2008**, *14* (9), 1527−1537.
(83) Park, S.-H. H.; Gil, E. S.; Cho, H.; Mandal, B. B.; Tien, L. W.; Min, B. H.; Kaplan, D. L. Intervertebral Disk Tissue Engineering Using Biphasic Silk Composite Scaffolds. *Tissue Eng., Part A* **2012**, *18* (5−6), 447−458.
(84) Zhuang, Y.; Huang, B.; Li, C. Q.; Liu, L. T.; Pan, Y.; Zheng, W. J.; Luo, G.; Zhou, Y. Construction of Tissue-Engineered Composite Intervertebral Disc and Preliminary Morphological and Biochemical Evaluation. *Biochem. Biophys. Res. Commun.* **2011**, *407* (2), 327−332.
(85) Balakrishnan, B.; Joshi, N.; Jayakrishnan, A.; Banerjee, R. Self-Crosslinked Oxidized Alginate/Gelatin Hydrogel as Injectable, Adhesive Biomimetic Scaffolds for Cartilage Regeneration. *Acta Biomater.* **2014**, *10* (8), 3650−3663.
(86) Fan, C.; Wang, D.-A. Potential Use of Alginate Beads as a Chondrocyte Delivery Vehicle and Stepwise Dissolving Porogen in a Hydrogel Scaffold for Cartilage Tissue Engineering. *RSC Adv.* **2015**, *5* (98), 80688−80697.
(87) Gloria, A.; De Santis, R.; Ambrosio, L.; Causa, F.; Tanner, K. E. A Multi-Component Fiber-Reinforced PHEMA-Based Hydrogel/HAPEX TM Device for Customized Intervertebral Disc Prosthesis. *J. Biomater. Appl.* **2011**, *25* (8), 795−810.
(88) Gansau, J.; Kelly, L.; Buckley, C. T. Influence of Key Processing Parameters and Seeding Density Effects of Microencapsulated Chondrocytes Fabricated Using Electrohydrodynamic Spraying. *Biofabrication* **2018**, *10* (3), 035011.

https://doi.org/10.1021/acsbiomaterials.1c01326
ACS Biomater. Sci. Eng. 2021, 7, 5836−5849